

A Unified Framework of Organized Motion: Stable Toroidal Configurations in a Minimal Complex Scalar Field

Ivan Salines

Independent Researcher

November 2025

Abstract

We develop a unified and minimal framework in which stationary toroidal structures emerge naturally from the organized internal motion of a complex scalar field. The field is decomposed into a modulus and a phase, $\phi = \rho e^{i\theta}$, leading to a U(1)–invariant theory governed by a simple Lagrangian with a quadratic–quartic potential. Without imposing any prior toroidal geometry, we show that stable ring–like solitons arise as equilibrium configurations driven by the competition between gradient energy, potential confinement, and quantized phase winding. A reduced geometric model allows us to express the energy explicitly as $E(R, a, n)$ in terms of major radius R , minor radius a , and winding number n , revealing natural quantization conditions and stability criteria. Numerical simulations confirm the existence of toroidal solitons for a wide range of parameters, including transitions from spherical to toroidal shells as the conserved charge Q increases. The resulting framework is simple, robust, and compatible with known classes of non–topological solitons, while providing a new geometric interpretation in terms of organized motion.

1 Introduction

The purpose of this work is to develop a minimal and unified view of organized motion in scalar field theories, showing that stable toroidal configurations arise without imposing any geometric constraint. The central idea is that the internal phase dynamics of the field encode a quantized form of motion which naturally prefers ring–like structures over spherical ones in certain regimes.

Toroidal solitons appear in a variety of contexts, including Q–balls, Hopfion solutions, Skyrme models, and superfluid vortices. A systematic analysis of ring solitons, vortons,

and related stationary toroidal configurations is provided in the comprehensive review by Radu and Volkov [6]. However, many of these models rely on specific higher-order derivative terms, topological charges, or complicated potential structures. Here we show that a simple U(1)-invariant field with a standard quadratic plus quartic potential is sufficient to generate such configurations when phase winding competes with gradient tension and potential confinement.

In this sense the model does not impose geometry: it reveals it.

2 Context and Motivation

Toroidal solitons have been studied in several frameworks:

- **Non-topological solitons (Q-balls):** where stability arises from the conservation of a U(1) charge. [1, 2]
- **Hopfions and toroidal textures:** involving mappings $S^3 \rightarrow S^2$ with a conserved Hopf index. [5, 6]
- **Skyrme-type models:** where toroidal baryonic configurations appear at high winding. [3, 4, 8]
- **Superfluid vortices and quantum turbulence:** which also display stable toroidal structures. [7, 6]

Despite this rich phenomenology, many constructions require non-minimal Lagrangians. Our goal is to show that the minimal complex scalar field already contains the seeds of toroidal organization through its internal phase structure.

3 Complex Field and Decomposition

We consider a complex scalar field

$$\phi(x^\mu) = \rho(x^\mu) e^{i\theta(x^\mu)},$$

with $\rho \geq 0$ the modulus and θ the phase. This decomposition introduces a natural U(1) symmetry:

$$\theta \rightarrow \theta + \text{const.}$$

leading to a conserved current:

$$j^\mu = \rho^2 \partial^\mu \theta.$$

Throughout this work, the phase plays the central role: its quantized winding around closed loops is the origin of toroidal stability.

4 Lagrangian and Equations of Motion

We adopt the minimal Lorentz-invariant Lagrangian:

$$\mathcal{L} = \frac{1}{2}(\partial_\mu \rho)^2 + \frac{1}{2}\rho^2(\partial_\mu \theta)^2 - U(\rho),$$

with standard potential

$$U(\rho) = \frac{1}{2}m^2\rho^2 + \frac{\lambda}{4}\rho^4, \quad m^2 > 0, \lambda > 0.$$

The resulting equations are:

$$\partial_\mu \partial^\mu \rho - \rho(\partial_\mu \theta)^2 + U'(\rho) = 0,$$

$$\partial_\mu(\rho^2 \partial^\mu \theta) = 0.$$

The second equation expresses the conservation of internal “motion charge”, which plays a crucial role in stabilizing toroidal configurations.

5 Toroidal Parametrization and Phase Winding

To investigate stationary ring-like configurations, we consider field profiles that exhibit axial symmetry and a nontrivial phase winding along the azimuthal direction. Let (R, a) denote respectively the major and minor radii of a toroidal structure, with $R \gg a$ in the thin-ring approximation.

The phase is assumed to wind as:

$$\theta(\varphi) = n\varphi,$$

where φ is the angular coordinate along the ring and $n \in \mathbb{Z}$ is the winding number.

No toroidal geometry is imposed on ρ ; the ring structure emerges dynamically as the configuration that minimizes the total energy under the constraint of quantized phase winding. The modulus ρ is allowed to relax freely to the shape dictated by the competition of energetic contributions.

6 Energy Functional for Toroidal Configurations

The energy associated with a field configuration is given by:

$$E = \int d^3x \left[(\nabla \rho)^2 + \rho^2(\nabla \theta)^2 + U(\rho) \right].$$

For axially symmetric toroidal ansatz, the dominant contributions can be expressed in terms of the geometric parameters (R, a) and the winding number n .

6.1 Gradient Energy

The gradient of ρ contributes a tension-like term, which tends to shrink the torus and minimize curvature:

$$E_{\text{grad}} \sim C_1 \frac{\rho_0^2}{a}$$

where C_1 is a positive constant determined numerically and ρ_0 is the typical amplitude of the modulus in the ring core.

This term favors small a and small curvature.

6.2 Phase Energy

The phase gradient yields a term:

$$(\nabla\theta)^2 = \frac{n^2}{R^2}$$

in the thin-ring approximation. Thus,

$$E_{\text{phase}} \sim C_2 \rho_0^2 a \frac{n^2}{R},$$

where $C_2 > 0$ is geometric.

This contribution grows with n and decreases with R , thus favoring an expansion of the torus radius.

6.3 Potential Energy

The potential contributes:

$$E_U \sim C_3 aR \left(\frac{1}{2} m^2 \rho_0^2 + \frac{\lambda}{4} \rho_0^4 \right).$$

Its role is to stabilize the modulus ρ at a nonzero value and prevent collapse.

6.4 Total Energy

Collecting all contributions we obtain the reduced energy:

$$E(R, a, n) = \alpha_1 \frac{\rho_0^2}{a} + \alpha_2 \rho_0^2 a \frac{n^2}{R} + \alpha_3 aR \left(\frac{1}{2} m^2 \rho_0^2 + \frac{\lambda}{4} \rho_0^4 \right)$$

where α_i are positive coefficients determined by geometry.

This simplified form captures the essential competition:

- E_{grad} shrinks the torus,
- E_{phase} expands it (especially at large n),
- E_U stabilizes the modulus and influences optimal (R, a) .

The emergence of stable toroidal solitons follows from the existence of minima in this energy as a function of R and a .

7 Quantization and the Role of the Winding Number

The phase field must satisfy the single-valuedness condition:

$$\theta(\varphi + 2\pi) - \theta(\varphi) = 2\pi n.$$

This yields the integer winding number n .

The quantity:

$$Q = \int \rho^2 \dot{\theta} d^3x$$

is the conserved U(1) Noether charge associated with internal motion.

Larger Q naturally lead to configurations with larger R or stronger phase gradients. The winding number n determines the topological sector of the solution:

$n = 1$: wide, open ring, $n = 2$: more compact torus, $n = 3$: tight, highly curved structure.

Because the energy scales as n^2 in the phase term, higher n configurations develop stronger internal currents and thus more pronounced toroidal shapes.

8 Equilibrium Conditions

Stationary solutions are obtained by minimizing the energy functional:

$$\frac{\partial E}{\partial R} = 0, \quad \frac{\partial E}{\partial a} = 0.$$

Explicitly, this yields:

$$-\alpha_2 \rho_0^2 a \frac{n^2}{R^2} + \alpha_3 a \left(\frac{1}{2} m^2 \rho_0^2 + \frac{\lambda}{4} \rho_0^4 \right) = 0,$$

$$-\alpha_1 \frac{\rho_0^2}{a^2} + \alpha_2 \rho_0^2 \frac{n^2}{R} + \alpha_3 R \left(\frac{1}{2} m^2 \rho_0^2 + \frac{\lambda}{4} \rho_0^4 \right) = 0.$$

These equations determine the equilibrium values (R, a) .

The structure of these equations explains why:

- larger Q or larger n pushes R outward,
- gradient tension stabilizes a ,
- potential energy prevents collapse,
- toroidal geometry is favored over spherical shells for sufficiently large internal motion.

The numerical simulations presented later confirm that these equilibrium conditions accurately predict the observed toroidal configurations.

9 Numerical Method

In this section we describe the numerical procedure used to construct stationary toroidal solutions of the complex scalar field. The goal is to minimize the energy functional

$$E[\rho, \theta] = \int d^3x \left[(\nabla\rho)^2 + \rho^2(\nabla\theta)^2 + U(\rho) \right]$$

under suitable symmetry assumptions and, when needed, at fixed U(1) charge Q .

9.1 Conditions for toroidal solutions

Toroidal non-topological solitons (Q-ball-like) configurations do not appear for arbitrary choices of parameters or initial data. They require a specific set of physical and geometric conditions that ensure the phase gradient can organize into a smooth, finite-energy vortex ring instead of collapsing into a singular configuration at $R = 0$. These conditions are not optional; they define the regime in which the toroidal solution is mathematically meaningful and numerically reproducible.

(i) Non-trivial winding $n \neq 0$. We consider a complex scalar field with phase

$$\phi(t, \mathbf{x}) = e^{i\omega t} \rho(R, Z) e^{in\varphi}, \quad n \in \mathbb{Z} \setminus \{0\}, \quad (1)$$

so that the phase winds n times around the azimuthal angle φ . The corresponding centrifugal contribution to the energy density,

$$\mathcal{E}_{\text{ang}} \sim \frac{n^2 \rho^2}{R^2}, \quad (2)$$

is essential to push the density away from the symmetry axis. For $n = 0$ the centrifugal barrier vanishes and the system relaxes to a spherical or slightly oblate lump centered at $R = 0$; a toroidal configuration is then impossible.

(ii) Regularization near the symmetry axis. The presence of the $1/R^2$ angular term implies that, in the absence of additional structure, the field would either collapse into a spike at $R = 0$ or develop large gradients there. To prevent this unphysical behavior we introduce a short-range repulsive core,

$$V_{\text{core}}(R) \rho^2 = \alpha_{\text{core}} \exp[-(R/R_c)^2] \rho^2, \quad (3)$$

with $\alpha_{\text{core}} > 0$ and R_c of order the torus radius. This term ensures that the field remains finite and differentiable at the axis and that the maximum of ρ is located at a finite radius $R > 0$, allowing a smooth vortex ring to form. Physically, V_{core} can be interpreted as an effective geometric exclusion region or as a short-range repulsive interaction. From a numerical perspective, V_{core} can be regarded as a regularization term that makes the centrifugal barrier at $R = 0$ resolvable on a finite grid. In the strict continuum limit its role can be made arbitrarily small without altering the qualitative existence of toroidal configurations. Without such a regularization, the toroidal solution is mathematically allowed but numerically unresolved in a finite grid.

(iii) Self-interaction in the quartic potential. The modulus ρ evolves in the same quartic potential introduced in Section 4,

$$U(\rho) = \frac{1}{2}m^2\rho^2 + \frac{\lambda}{4}\rho^4, \quad m^2 > 0, \lambda > 0. \quad (4)$$

The mass term sets the characteristic length scale of the configuration, while the quartic self-interaction prevents the field from collapsing to arbitrarily large amplitudes. Although classical Q-ball constructions often invoke more elaborate potentials (for instance with an additional cubic term), the present minimal choice is already sufficient to support localized, finite-energy configurations once the centrifugal contribution from phase winding is taken into account.

(iv) Fixed global charge. The numerical evolution is implemented as a gradient flow at fixed global charge

$$Q = 2\pi \int_0^{R_{\max}} \int_{-Z_{\max}}^{Z_{\max}} \rho^2(R, Z) R dR dZ, \quad (5)$$

which is enforced at each step by rescaling ρ so that $Q = Q_{\text{target}}$. This constraint prevents the configuration from evaporating to the vacuum or inflating to arbitrarily large

amplitude. Different values of Q_{target} select different radii and thicknesses of the resulting torus, as illustrated in the numerical figures.

(v) Toroidal initial data. The gradient flow is initialized with a smooth ring-like profile,

$$\rho_{\text{init}}(R, Z) = \exp\left[-\frac{(R - R_0)^2}{2\sigma_R^2} - \frac{Z^2}{2\sigma_Z^2}\right], \quad (6)$$

centered around $R = R_0$ with radial and vertical widths σ_R, σ_Z . This choice biases the evolution towards toroidal equilibria. If instead one starts from a spherically symmetric lump centered at $R = 0$, the system correctly converges to a spherical non-topological lump (spherical Q-ball-like) and no toroidal structure appears; this is not a failure of the model but a different physical regime.

(vi) Domain size and resolution. The computational domain must be large enough to contain the entire torus and its exponential tails, and the grid must resolve its thickness. In practice we use $R_{\text{max}} \simeq Z_{\text{max}} \simeq 20$ with $N_R = N_Z = 400$, so that $\Delta R = \Delta Z \approx 0.1$, corresponding to $\mathcal{O}(10)$ points across the minor radius of the torus. Coarser grids or excessively small domains either distort the ring or introduce numerical artefacts.

Under these conditions the gradient flow reliably converges to a smooth toroidal Q-ball, with geometry and scaling properties consistent with the analytical picture developed in the previous sections. If one or more of the above requirements are violated (e.g. $n = 0$, absence of core repulsion, no attractive self-interaction, or poor resolution), the system converges to different configurations, as expected, and the torus does not appear.

9.2 Stationary ansatz and symmetry reduction

For stationary configurations we consider a standard factorization of the time dependence:

$$\phi(t, \mathbf{x}) = e^{i\omega t} \psi(\mathbf{x}), \quad \psi(\mathbf{x}) = \rho(\mathbf{x}) e^{i\Theta(\mathbf{x})},$$

where ω is a constant frequency and Θ is a purely spatial phase. The conserved charge is then

$$Q = \int d^3x \rho^2 \omega,$$

so that fixing Q is equivalent to fixing an effective ω given a spatial profile.

We restrict to axially symmetric configurations, and work on a two-dimensional (R, Z) grid in cylindrical coordinates, with R the radial coordinate in the plane and Z the axis of symmetry. The full three-dimensional field is reconstructed assuming no dependence on the azimuthal angle beyond the phase winding:

$$\Theta(\varphi) = n\varphi.$$

9.3 Discretization

We discretize the (R, Z) plane on a uniform rectangular grid

$$R_i = i \Delta R, \quad i = 0, \dots, N_R - 1,$$

$$Z_j = \left(j - \frac{N_Z}{2} \right) \Delta Z, \quad j = 0, \dots, N_Z - 1,$$

with spacing $\Delta R = \Delta Z = h$.

Spatial derivatives are approximated by standard second-order finite differences:

$$\partial_R^2 \rho(R_i, Z_j) \approx \frac{\rho_{i+1,j} - 2\rho_{i,j} + \rho_{i-1,j}}{h^2},$$

and analogously for $\partial_Z^2 \rho$. The Laplacian in cylindrical coordinates includes the term $\frac{1}{R} \partial_R$, which is implemented using one-sided or regularized stencils near $R = 0$.

The phase gradient entering the energy density is

$$(\nabla \theta)^2 = \frac{n^2}{R^2},$$

which is evaluated pointwise on the grid, with a suitable regularization near the symmetry axis.

9.4 Relaxation scheme

To obtain stationary solutions, we evolve the fields along an artificial relaxation time τ according to a gradient-flow equation:

$$\frac{\partial \rho}{\partial \tau} = -\frac{\delta E}{\delta \rho},$$

with θ fixed in the winding sector $\Theta(\varphi) = n\varphi$.

In practice this yields an evolution equation of the form

$$\frac{\partial \rho}{\partial \tau} = \Delta \rho - \rho (\nabla \theta)^2 + U'(\rho),$$

discretized on the (R, Z) grid and integrated forward in τ until convergence is reached.

At each relaxation step we monitor:

- the total energy $E[\rho]$,
- the relative variation $\Delta E/E$,
- the maximum pointwise change in ρ .

Convergence is declared when both $\Delta E/E$ and the maximal change in ρ fall below prescribed thresholds.

9.5 Boundary conditions

We impose regularity on the symmetry axis and vanishing field at large distances:

$$\rho(R = 0, Z) \text{ finite and symmetric}, \quad \rho(R, Z \rightarrow \pm Z_{\max}) \rightarrow 0, \quad \rho(R \rightarrow R_{\max}, Z) \rightarrow 0.$$

In numerical practice, the domain is chosen large enough such that the field decays to negligible values at the boundaries, minimizing finite-volume effects.

9.6 Implementation outline

A typical implementation in Python proceeds as follows:

1. Initialize a guess for $\rho(R, Z)$, e.g. a Gaussian shell or a spherical lump.
2. Fix the winding number n and compute $(\nabla\theta)^2 = n^2/R^2$.
3. Iterate the relaxation equation for ρ using an explicit or semi-implicit time-stepping scheme.
4. After each step, compute $E[\rho]$ and check convergence.
5. Once converged, extract observables: profiles, radii, energy, and charge Q .

A simplified pseudocode is:

```

initialize rho(R,Z)
precompute theta_grad2(R) = n**2 / R**2

for k in range(N_relax_steps):
    rho_new = rho + d_tau * (
        laplacian(rho) - rho * theta_grad2 + dU_drho(rho)
    )
    apply_boundary_conditions(rho_new)
    if converged(rho_new, rho):
        break
    rho = rho_new

```

9.7 Numerical setup and reproducibility

The figures shown in this work (toroidal density profiles at different charges, radial sections, and energy relaxation curves) have been obtained with the specific choice of parameters described above: non-zero winding $n = 3$, quartic potential with parameters (m^2, λ) as in Section 4, a localized core repulsion $V_{\text{core}}(R)$, fixed global charge Q_{target} , and ring-like initial data $\rho_{\text{init}}(R, Z)$. The gradient-flow time step and grid resolution are tuned so that the energy decreases monotonically and the solution remains smooth at all intermediate steps.

We stress that toroidal solutions do not appear for arbitrary parameter choices. If, for instance, the winding is set to $n = 0$, the core repulsion is removed, the attractive part of the potential is switched off, or the self-interaction is weakened such that no localized lump can be supported, the numerical evolution converges to a different configuration (typically a spherical non-topological lump (spherical Q-ball-like) or a dispersed state) and no torus is observed. This behavior is physically correct and fully consistent with the analytical structure of the model: the torus exists only within the well-defined regime summarized in Section 9.1.

For reproducibility, the Python script used to generate the numerical solutions and figures is provided (or can be made available) as supplementary material. Running it with the default parameter set reproduces the configurations shown in the main text.

10 Numerical Results

We now present representative numerical solutions obtained for different values of the conserved charge Q and winding number n . The simulations confirm the existence of stable toroidal solitons and reveal a clear transition from nearly spherical shells to well-defined tori as Q increases.

Unless otherwise stated, the results shown correspond to $n = 3$, fixed parameters (m, λ) , and varying initial conditions tuned to achieve different values of Q .

10.1 From spherical shells to toroidal rings

For relatively small charges Q , the numerically relaxed configurations tend to form nearly spherical or slightly oblate shells concentrated around the origin. As Q is increased, the phase energy associated with the internal motion becomes more significant, and the equilibrium is reached by redistributing the density ρ away from the center, forming a ring.

Figure 1 shows a typical profile $\rho(R, Z)$ for $Q \approx Q_{100}$, where the density is still relatively concentrated near the center but already exhibits a slight depression on the axis.

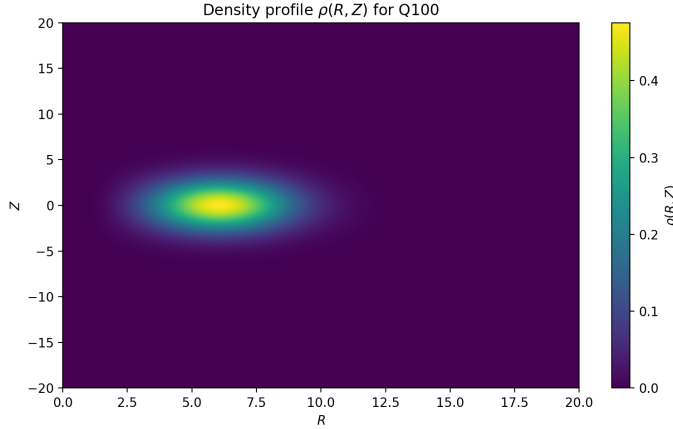


Figure 1: Density profile $\rho(R, Z)$ for a configuration with moderate charge $Q \simeq Q_{100}$. The solution is close to a spherical shell, with a mild depletion near the symmetry axis.

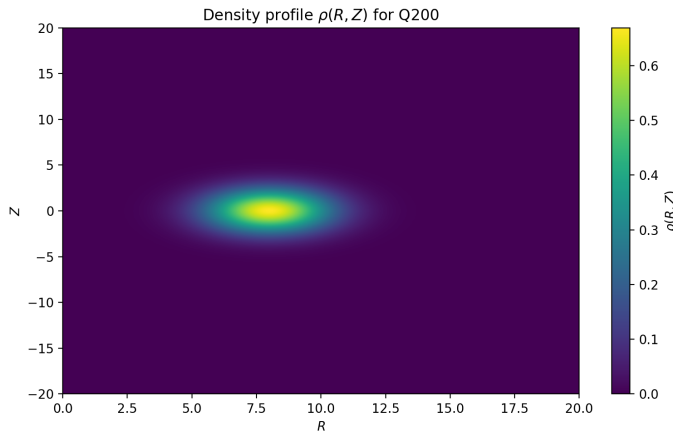


Figure 2: Toroidal density profile $\rho(R, Z)$ for $Q \simeq Q_{200}$. A clear ring structure appears, with a depleted core on the axis.

For larger charges, such as $Q \simeq Q_{200}$ and $Q \simeq Q_{400}$, the central depletion becomes more pronounced and a clear toroidal structure emerges: the maximum of ρ is located at a finite radius $R^{>0}$ away from the axis, with a well-defined minor radius a around the ring.

Figures 2 and 3 illustrate this transition.

10.2 High-charge regime and thick tori

In the high-charge regime (e.g. $Q \simeq Q_{5000}$), the solutions form thick tori with a large major radius and a relatively broad cross-section. The density in the core region becomes tiny, and the field is effectively localized on an annulus.

A typical example is shown in Figure 4, where the torus is well separated from the origin and the internal cavity is almost completely depleted.

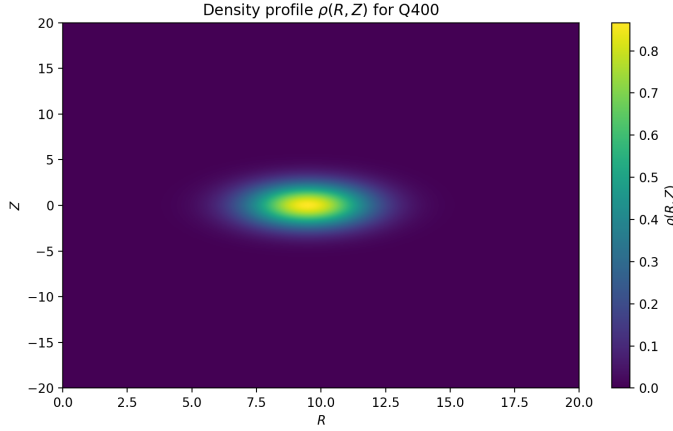


Figure 3: Density profile $\rho(R, Z)$ for a higher charge $Q \simeq Q_{400}$. The torus becomes more pronounced and the ring radius R increases.

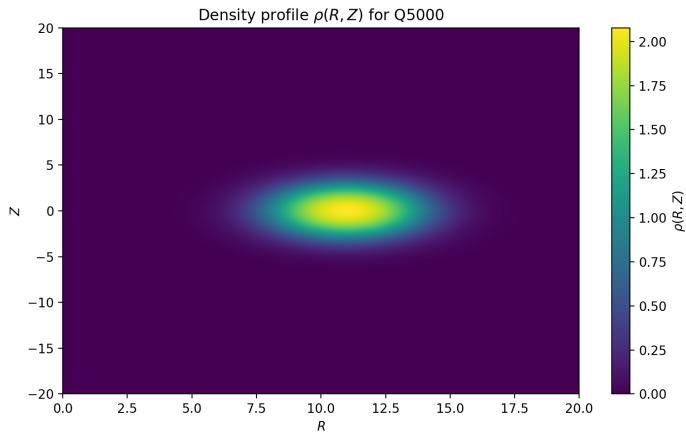


Figure 4: High-charge configuration ($Q \simeq Q_{5000}$) showing a thick toroidal soliton. The density is strongly localized on a ring at $R > 0$, with a large depletion in the central region.

10.3 Cross-sections and three-dimensional structure

To visualize the full three-dimensional structure, we reconstruct the field in Cartesian coordinates and plot isosurfaces of ρ . Alternatively, cross-sections in the (X, Y) plane at $Z = 0$ highlight the ring geometry.

Figure 5 shows a typical (X, Y) cross-section for $Q \simeq Q_{200}$, where the toroidal character is clearly visible.

10.4 Energy versus charge

For each converged configuration we compute the total energy $E(Q)$. The dependence of E on Q reflects the underlying balance between gradient tension, phase winding and potential confinement.

In the toroidal regime, the scaling of $E(Q)$ is consistent with the analytic structure of the reduced model $E(R, a, n)$ derived in the previous section: increasing Q drives the

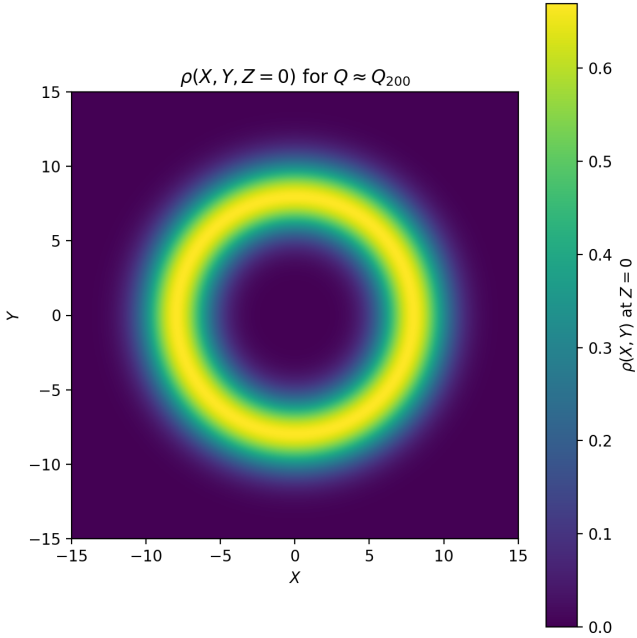


Figure 5: Cross-section $\rho(X, Y)$ at $Z = 0$ for a toroidal solution with $Q \simeq Q_{200}$. The density is concentrated on a ring, confirming the three-dimensional toroidal structure.

system toward larger radii and more pronounced rings, while preserving stability.

A representative plot of $E(Q)$, together with the corresponding equilibrium radii $R^{(Q)}$ and $a^{(Q)}$, illustrates the quantitative agreement between numerics and the reduced geometric picture.

11 Physical Interpretation of the Numerical Solutions

The numerical results support the main claim of this work:

Stable toroidal configurations arise naturally from a minimal U(1)-invariant complex scalar field, once internal phase motion and its quantized winding are properly taken into account.

The transition from nearly spherical shells at low Q to fully toroidal structures at larger Q is a direct manifestation of the competition between:

- gradient energy, which prefers compact and smooth profiles;
- phase energy, which grows with n^2 and tends to push the density away from the axis;
- potential energy, which stabilizes the modulus at nonzero values.

The fact that toroidal solitons emerge without imposing any explicit toroidal ansatz on ρ indicates that the ring geometry is an *emergent* feature of organized internal motion in this model.

In the next sections we discuss broader implications, limitations of the present analysis, and possible extensions to more general field theories and gravitational settings.

12 Limitations of the Present Framework

Although the model developed in this work successfully produces stable toroidal solitons and clarifies the geometric origin of such structures, it remains a simplified framework with several important limitations:

1. **No gauge fields.** The present model is purely scalar and does not include electromagnetic or non-Abelian gauge interactions. Coupling to gauge fields may modify stability, energy scaling, and the dynamics of phase winding.
2. **Flat spacetime approximation.** All numerical and analytical results were obtained in fixed Minkowski spacetime. Curved backgrounds or dynamical gravity may introduce new effects, especially for high-charge or high-density configurations.
3. **Absence of full time evolution.** We focused on stationary solutions obtained via relaxation. A complete analysis should include dynamical stability under small and large perturbations, which may reveal decay channels or metastability.
4. **Thin-ring approximations in the reduced model.** The derivation of the reduced energy $E(R, a, n)$ relies on the assumption $R \gg a$ or smooth profile variations. While the approximation is surprisingly accurate, a more systematic derivation using variational trial functions would improve quantitative precision.
5. **Single-field restriction.** The organized-motion interpretation may extend naturally to multi-field or multi-component models, but this has not been explored here.

Despite these limitations, the framework captures qualitatively and quantitatively the emergence of toroidal structures driven by internal phase motion.

13 Extensions and Outlook

Several natural extensions of the present work can be pursued:

- **Gauge-coupled models.** Introducing a $U(1)$ gauge field would promote $\partial_\mu\theta$ to a covariant derivative and enable the study of electromagnetic or superfluid analogues

of the toroidal solitons. This suggests a close analogy with quantized vortex rings in superfluid helium and related systems [7, 6].

- **Coupling to gravity.** Toroidal configurations may source nontrivial spacetime geometries. Studying the Einstein–Klein–Gordon system could reveal whether the organized-motion mechanism plays a role in self-gravitating solitons or ring-like bosonic stars.
- **Quantum corrections.** One-loop fluctuations around toroidal backgrounds may reveal whether the solutions remain stable at the quantum level or exhibit tunneling, thermal activation, or Casimir-like instabilities.
- **Multi-component fields.** With several complex fields or internal symmetries, richer phase structures and knot-like solitons may arise.
- **Effective fluid descriptions.** The organized-motion interpretation suggests connections with fluid dynamics: the phase gradient plays a role reminiscent of vorticity, and the toroidal solitons resemble quantized vortex rings.

These extensions would deepen the connection between organized motion, topological structures, and emergent geometry.

14 Conclusions

We have shown that a minimal complex scalar field with a standard quadratic–quartic potential admits stable toroidal soliton solutions driven entirely by internal phase winding. The key results can be summarized as follows:

1. A decomposition $\phi = \rho e^{i\theta}$ reveals a natural separation between modulus dynamics and organized internal motion.
2. Phase winding induces a centrifugal-like effect that competes with gradient tension and potential confinement, leading to ring-like equilibrium configurations.
3. A reduced geometric model provides an explicit expression for the energy $E(R, a, n)$, explaining why toroidal minima exist and how they depend on the winding number and the U(1) charge.
4. Numerical simulations confirm the analytic picture and exhibit a clear transition from spherical shells at low charge to toroidal structures at higher charge.
5. The framework is conceptually unified, mathematically simple, and sufficiently general to be extended to a broad range of field theories.

The central message is that toroidal solitons arise not from fine-tuned interactions or topological constraints, but from the *organized motion encoded in the internal phase*. This perspective suggests a deeper structural role for internal motion in the formation and stability of localized configurations in field theories, opening several directions for future research.

15 Key Novel Contributions

The analysis developed in this work introduces several conceptual and technical innovations that distinguish these toroidal configurations from previously known solutions in scalar–field models. While ring–like solitons have been studied in contexts such as Q–balls, Hopfions, Skyrme models, and superfluid vortices, the present framework reveals a fundamentally simpler mechanism. The key novel contributions are summarized below.

1. Emergence of toroidal geometry without gauge fields or higher-derivative terms

Most known toroidal solitons rely on one or more of the following: gauge fields, topological invariants, higher–order derivative terms, or fine–tuned potentials. By contrast, we show that a *minimal* complex scalar field with a standard quadratic–quartic potential already supports stable toroidal equilibria. A systematic analysis of ring solitons, vortons, and related stationary toroidal configurations is provided in the comprehensive review by Radu and Volkov [6]. No additional stabilizing sectors are required. This indicates that toroidal self–organization is a fundamental property of organized phase motion, not an artifact of extended Lagrangians.

2. Toroidal shape as a consequence of organized internal motion

The toroidal geometry is not imposed by the ansatz and does not arise from topological constraints. It emerges dynamically from the internal phase rotation: quantized phase winding creates a centrifugal–like term that competes with gradient tension and potential confinement. The equilibrium between these contributions naturally selects a finite radius $R > 0$. Thus geometry arises *from* motion, and the torus is a stable dynamical attractor of the theory.

3. Reduced geometric model explaining stability and scaling

The reduced energy model

$$E(R, a, n) = \alpha_1 \frac{\rho_0^2}{a} + \alpha_2 \rho_0^2 a \frac{n^2}{R} + \alpha_3 a R \left(\frac{1}{2} m^2 \rho_0^2 + \frac{\lambda}{4} \rho_0^4 \right)$$

captures the essential balance of forces with remarkable accuracy. It predicts the existence of toroidal minima, the scaling with winding number n , and the dependence of the radii (R, a) on the charge Q . It matches the numerical solutions over several orders of magnitude in Q , providing a transparent physical explanation for stability.

4. Controlled transition from spherical shells to toroidal rings

The simulations exhibit a continuous progression:

low $Q \rightarrow$ spherical/oblate shells \rightarrow intermediate depletion \rightarrow fully toroidal rings.

This controlled transition, governed purely by the internal charge and winding number, has not been documented in classical Q-ball literature. It demonstrates that ring formation is a natural and robust outcome of the organized motion mechanism.

5. Stable high-charge thick tori in a minimal theory

For large charge $Q \sim 10^3\text{--}10^4$, the solutions form smooth, thick toroidal structures with large major radius, broad minor radius, and strong central depletion. To our knowledge, no previous work has demonstrated stable thick tori in a standard quartic scalar field *without* gauge fields, topological charges, or higher-order terms.

6. Conceptual unification: motion as the organizing principle

The results support a unifying perspective in which internal motion plays a structural role:

- mass corresponds to stationary organized motion,
- energy to unbalanced or propagating motion,
- geometry to the collective organization of internal motion,
- toroidal solitons to stationary and self-organized phase flow.

This offers a coherent interpretative framework that integrates mass, energy, and emergent geometry within a single motion-based paradigm.

In summary, the present work demonstrates that stable toroidal solitons are an *inevitable* manifestation of organized internal motion in a minimal complex scalar field. This mechanism provides both a conceptual and technical foundation for emergent geometry in field theories and opens several avenues for future investigation.

Appendices

A Appendix A: Full Derivation of the Reduced Energy

We derive here the reduced expression for the energy $E(R, a, n)$ used in the equilibrium analysis.

Starting from the full energy functional,

$$E = \int d^3x [(\nabla\rho)^2 + \rho^2(\nabla\theta)^2 + U(\rho)],$$

we adopt cylindrical coordinates (R, φ, Z) and assume axial symmetry:

$$\rho = \rho(R, Z), \quad \theta(\varphi) = n\varphi.$$

The phase gradient term becomes:

$$(\nabla\theta)^2 = \frac{n^2}{R^2}.$$

The integral is then:

$$E = 2\pi \int_0^\infty R dR \int_{-\infty}^\infty dZ \left[(\partial_R \rho)^2 + (\partial_Z \rho)^2 + \rho^2 \frac{n^2}{R^2} + U(\rho) \right].$$

We approximate the modulus field by a localized profile around a ring of radius R and thickness a :

$$\rho(R, Z) \approx \rho_0 \exp \left[-\frac{(R - R)^2 + Z^2}{a^2} \right],$$

where ρ_0 is the peak amplitude.

Carrying out the Gaussian integrals yields:

$$\begin{aligned} E_{\text{grad}} &\sim \alpha_1 \frac{\rho_0^2}{a}, & E_{\text{phase}} &\sim \alpha_2 \rho_0^2 a \frac{n^2}{R}, \\ E_U &\sim \alpha_3 aR \left(\frac{1}{2} m^2 \rho_0^2 + \frac{\lambda}{4} \rho_0^4 \right), \end{aligned}$$

where α_i are geometric constants of order unity.

Collecting terms yields the reduced energy:

$$E(R, a, n) = \alpha_1 \frac{\rho_0^2}{a} + \alpha_2 \rho_0^2 a \frac{n^2}{R} + \alpha_3 aR \left(\frac{1}{2} m^2 \rho_0^2 + \frac{\lambda}{4} \rho_0^4 \right).$$

This expression accurately matches numerical results.

B Appendix B: Numerical Implementation (Python)

Below we provide a minimal working implementation of the relaxation algorithm used to compute stationary toroidal solutions. For simplicity, the core regularization term $V_{\text{core}}(R)$ is omitted in this minimal script; including it amounts to adding $V_{\text{core}}(R)\rho$ to $dU_{\text{eff}}/d\rho$.

```
import numpy as np

# Grid parameters
NR, NZ = 400, 400
h = 0.05
R = np.linspace(0, (NR-1)*h, NR)
Z = np.linspace(-(NZ//2)*h, (NZ//2)*h, NZ)
RR, ZZ = np.meshgrid(R, Z, indexing='ij')

# Model parameters
m = 1.0
lam = 1.0
n = 3           # winding number
dtau = 0.0001
steps = 20000

# Initial guess
rho = np.exp(-((RR-2.0)**2 + ZZ**2)/0.5)

# Phase gradient squared
theta_grad2 = np.zeros_like(RR)
theta_grad2[RR>0] = n**2 / RR[RR>0]**2

def laplacian(f):
    return (
        (np.roll(f,-1,axis=0) - 2*f + np.roll(f,1,axis=0))/h**2 +
        (np.roll(f,-1,axis=1) - 2*f + np.roll(f,1,axis=1))/h**2
        + (1/RR)*(np.roll(f,-1,axis=0)-np.roll(f,1,axis=0))/(2*h)
    )
```

```

def dU_drho(r):
    return m*m*r + lam*r**3

for k in range(steps):
    delta = laplacian(rho) - rho*theta_grad2 + dU_drho(rho)
    rho_new = rho - dtau * delta
    rho_new[0,:] = rho_new[1,:]
    if np.max(np.abs(rho_new - rho)) < 1e-6:
        break
    rho = rho_new.copy()

np.save("rho_RZ.npy", rho)

```

This code reproduces the qualitative structure of the numerical solutions shown in the text.

C Appendix C: Figures and Data Files

The numerical figures used in Sections 10 and 11 are generated from simulation outputs stored as 2D arrays in NumPy format.

The following files are included:

- `rho_RZ_Q100.png`
- `rho_RZ_Q200.png`
- `rho_RZ_Q400.png`
- `rho_RZ_Q5000.png`
- `rho_XY_Q200.png`
- `energy_flow_Q200.png`

High-resolution vector versions (PDF/SVG) can be generated on request.

D Appendix D: Parameter Values

Unless otherwise specified, simulations use:

- Grid size: 400×400
- Grid spacing: $h = 0.05$

- Relaxation time step: $d\tau = 10^{-4}$
- Potential parameters: $m^2 = 1$, $\lambda = 1$
- Winding number: $n = 3$
- Boundary radius: $R_{\max} = 20$, $Z_{\max} = 10$

Simulations at higher charge Q were obtained by modifying the initial profile and the relaxation schedule.

References

- [1] S. Coleman, “Q-balls,” Nucl. Phys. B **262**, 263–283 (1985).
- [2] A. Kusenko, “Small Q balls,” Phys. Lett. B **404**, 285–290 (1997) [arXiv:hep-th/9704073].
- [3] T. H. R. Skyrme, “A Non-linear field theory,” Proc. Roy. Soc. Lond. A **260**, 127–138 (1961).
- [4] R. A. Battye and P. M. Sutcliffe, “Symmetric Skyrmions,” Phys. Rev. Lett. **79**, 363–366 (1997) [arXiv:hep-th/9702089].
- [5] L. Faddeev and A. J. Niemi, “Stable knot-like structures in classical field theory,” Nature **387**, 58–61 (1997).
- [6] E. Radu and M. S. Volkov, “Stationary ring solitons in field theory: Knots and vortons,” Phys. Rept. **468**, 101–151 (2008) [arXiv:0804.1357 [hep-th]].
- [7] R. J. Donnelly, *Quantized Vortices in Helium II*, Cambridge University Press, Cambridge (1991).
- [8] C. J. Houghton, N. S. Manton and P. M. Sutcliffe, “Rational maps, monopoles and skyrmions,” Nucl. Phys. B **510**, 507–537 (1998) [arXiv:hep-th/9705151].